Effective Ag doping and resistance to sulphur poisoning of La-Mn perovskites for the catalytic flameless combustion of methane

O. Buchneva[a], I. Rossetti[a*], C. Oliva[a], M. Scavini[a], S. Cappelli[a], B. Sironi[a], M. Allieta[a], A. Kryukov[b], L. Forni[a]

[a)] Dip. Chimica Fisica ed Elettrochimica, Università di Milano, v. C. Golgi, 19, 20133 Milano, Italy

[b)] D.I.Mendeleev University of Chemical Technology of Russia, Miusskaya sq. 9. 125047, Moscow, Russia

ABSTRACT

Perovskite-like structured catalysts showed satisfactory activity for the low temperature flameless combustion of methane. This process allows to decrease the emission of CO, NO_x and unburnt hydrocarbons. Partial metal ions substitution in the composition of perovskites may improve catalytic activity and it can modulate their resistance to sulphur poisoning. Silver is an interesting dopant due to its limited solubility in the perovskite structure and suitable activity both in extra- and intra-framework position. The amount of lattice silver tightly depends on the preparation procedure.

Samples with nominal composition $La_{1-x}Ag_xMnO_{3\pm\delta}$ with x = 0; 0.05; 0.10 were prepared by flame spray pyrolysis (FP) and by the so-called sol-gel citrate method (SG). Temperature-programmed analysis, X-ray powder diffraction (XRPD) and Electron Paramagnetic Resonance (EPR) spectroscopy were used as main characterisation tools. Almost all of the catalysts showed very active for the flameless combustion of methane. The activity of the FP-prepared catalysts was always higher than that of the SG-prepared ones with identical nominal composition. Furthermore, partial substitution of Ag for La led

* Corresponding author: Fax +39-02-50314300; e-mail: ilenia.rossetti@unimi.it.

to substantially higher activity both for SG- and FP-prepared catalysts and the catalytic activity increased with increasing Ag substitution. The residual activity after poisoning with tetrahydrothiophene, a common odoriser used in the natural gas grid, is also presented, together with the transient response of the samples upon poisoning.

1 - INTRODUCTION

$La_{1-x}A'_xMnO_{3\pm\delta}$ perovskite-like materials (in particular with A'= Ca, Sr) are known since many decades. In the '90s a renewed interest has grown for these systems because of their properties of Giant Magnetoresistance, as well as because of other interesting transport properties [1-12], such as oxygen transport, important for their activity as catalysts in the catalytic flameless combustion (CFC) of methane [10-12] and for solid oxide fuel cells. Transport properties are strongly dependent on the nature of the ions partially substituting for La^{3+} [11] as well as on the preparation procedure [12]. Manganite perovskites may be valuable catalysts for the CFC of hydrocarbons, provided a proper preparation method is used, leading to suitable thermal resistance and catalytic activity. Flame Spray Pyrolysis (FP) [13] proved a promising technique from both points of view, leading to pure oxide nanopowder, calcined within the flame for a few milliseconds at 1200-1800°C, depending on the operating conditions.

Very recently, we also focused our attention on the resistance to poisoning by sulphur containing compounds. At difference with previous investigations, mainly dealing with catalytic mufflers, we selected tetrahydrothiophene (THT) as poison, due to its wide use as odorising agent in the methane distribution grid, where its concentration is *ca*. 8 ppmv [14, 15].

In general, the partial substitution of the perovskite-like lattice metal ions is one of the important means to modulate catalytic activity. In $LaBO_3$ perovskites, the influence of dopants such as A'^{2+} and A'^{4+} has been widely investigated in the literature [16-19].

Depending on the nature of the B metal ion, the former substituent can lead to the partial oxidation of the B ion, whereas the latter can lead to its partial reduction or, as in the case of manganites, to oxygen overstoichiometry. Moreover, in a previous investigation on silver doping [20] it was found that in $Sr_{1-x}Ag_xTiO_{3\pm\delta}$ perovskites silver may exist either as intra-crystalline framework Ag^+ and Ag^{2+} ions or as inter-crystalline metallic silver. Ag^{2+} ions could interact with some O_x^- species, leading to O_x^-/Ag^{+2} couples, so affecting oxygen mobility and catalytic activity. However, a much lower Ag^{2+} substitution degree occurred for samples prepared by flame-based techniques, *i.e*. flame pyrolysis (FP) and flame hydrolysis (FH) [20], with respect to samples obtained via sol–gel (SG) synthesis. This is a consequence of the milder preparation conditions achieved with the latter procedure, allowing the perovskite lattice to allocate a higher amount of extraneous ions. Therefore, partial substitution of Ag for La excites interest paradoxically due to the limited solubility of the former in the perovskite lattice. Indeed, it can partially allocate as extraframework metallic silver with its own possible catalytic activity, the degree of substitution depending on the preparation procedure and on the thermal treatment [21-23].

On the basis of recent results on Ag-doped $LaCoO_3$ samples, the effect of Ag substitution can be summarised as follows. If the concentration of silver is low, it can be quite fully incorporated into the perovskite lattice, possibly leading to an improved mobility of lattice oxygen (*i.e*. increased amount of oxygen vacancies) with increasing catalytic activity. By raising silver loading, it can turn into extraframework position, partly in the metallic state. Based on many investigations on the interaction between oxygen and metallic silver particles of variable size, a suitable activity is expected for bigger particle size, releasing oxygen at moderately low temperature [24-27]. By contrast, small Ag crystallites lead to stronger Ag-O bond, so decreasing the number of active sites for low temperature methane oxidation [28].

In the present investigation we compared $La_{1-x}A'_xMnO_{3\pm\delta}$ samples with A'=Ag and *x* = 0; 0.05; 0.10, prepared by FP, to samples with the same composition, but prepared by SG. Comparative samples obtained by impregnation of Ag on SG or FP-$LaMnO_3$ have been also prepared. Temperature-programmed analysis, X-ray powder diffraction (XRPD) and Electron Paramagnetic Resonance (EPR) spectroscopy have been employed to characterise all the catalysts and to investigate the effect of Ag doping and of preparation procedure on their catalytic performance for the CFC of methane. The resistance to sulphur poisoning was also analysed in view of practical application.

2 – EXPERIMENTAL

2.1 - Catalysts preparation

The present samples were prepared by flame pyrolysis (FP) and by a modified version of the SG method, as described here below. Since only partial Ag incorporation in the $LaMnO_3$ lattice can be reached (*vide infra*), the formula $La_{1-x}Ag_xMnO_3$ should be better represented by y-Ag/$La_{1-x-y}Ag_xMnO_3$, where *x* represents the fraction of Ag incorporated into the perovskite framework, whereas *y* is the Ag molar fraction in extraframework position. However, to avoid complex notations, the nominal composition only will be used in the following. Samples labelled as 10%Ag/$LaMnO_3$ were prepared by wet impregnation of the undoped perovskite from an aqueous solution of $AgNO_3$.

2.1.1 - Flame pyrolysis

Clear solutions were prepared with salts of the selected metals $La(CH_3COO)_3 \cdot 2H_2O$ (Aldrich, pur. 99.9%), $Mn(CH_3COO)_2 \cdot 4H_2O$ (Aldrich, pur. 99%), $Ag(CH_3COO)$ (Fluka, pur. ≥99%) in the desired ratio and metal concentration. The selected solvent (fuel) was propionic acid (Aldrich, pur. 97%). The solution was co-fed with pure oxygen to the FP apparatus described in detail in [13].

2.1.2 - Sol-gel method

Appropriate amounts of manganese and silver nitrates were dissolved in a small amount of distilled water, so to obtain a concentrated solution. Lanthanum carbonate was dissolved in diluted nitric acid. The solutions were mixed and the complexing agent (citric acid) was added in a 50 mol% excess with respect to the molar sum of the metals. After evaporation of the solvent at 80°C in rotavapor a free-flowing powder was obtained. Then, the powder was calcined at 300°C for 1h, and at 550°C and 700°C, for 3h at each temperature.

2.2 - Catalyst characterisation

The crystal structure was determined by XRPD on a Philips PW3020 diffractometer operating with Ni-filtered Cu-K_α radiation (λ=1.5418Å). Patterns were collected in the range $5° \leq 2\theta \leq 80°$ with $\Delta 2\theta = 0.02°$ steps and compared with literature data [29] for phase recognition. Rietveld refinements were carried out by the GSAS software [30] and its graphical interface EXPGUI [31]. Background has been subtracted using the shifted Chebyshev polynomials, whereas the diffraction peak profiles have been fitted with a modified pseudo-Voigt profile function. It should be noted that an accurate description of the line profile was difficult for the FP-prepared samples, due to the presence of bimodal

particle size distribution. In order to avoid over-parametrisation, in the last refinement just one line profile parameter (Lorentzian particle size broadening) was varied together with background parameters, cell constants, mean thermal parameter. The atomic site fractions have been fixed to the *nominal* values. Conversely, the site occupancy related to La^{3+} ions has been varied fixing the atomic site fraction of dopant ion to the *nominal* value for the SG $La_{1-x}Ag_xMnO_3$ samples, for which the bimodal particle size distribution was not observed,. The atomic fractional coordinates for the undoped and doped FP and SG $LaMnO_3$ samples have been taken from neutron powder diffraction investigations [32].

The specific surface area (SSA) of the synthesized powders was measured by N_2 adsorption/desorption at 77 K on a Micromeritics ASAP2010 apparatus, after outgassing *in vacuo* at 300°C overnight. The main properties of the prepared catalysts are summarised in Table 1.

Temperature-programmed analysis was carried out on *ca*. 0.15 g of catalyst in the same apparatus used for activity testing (*vide infra*). Sample pretreatment was performed in He (40 cm^3/min) while heating from room temperature (r.t.) up to 800°C (10°C/min), kept for 1h. Then, the sample was presaturated in flowing air at 750°C for 1h and cooled to r.t.. Temperature-Programmed Desorption of oxygen (O_2 – TPD) was carried out under the same conditions of the pretreatment, whereas Temperature-Programmed Reduction (TPR) was carried out after the same pretreatment and saturation, by flowing 40 cm^3/min of 10 vol% H_2 in He, while increasing temperature (10°C/min) from r.t. up to 800°C.

The EPR spectra have been collected at the working frequency of *ca*. 9.4 GHz on loose-packed samples, loaded in cylindric quartz tubes by means of a Bruker Elexsys spectrometer, equipped with an ER4102ST standard rectangular cavity and with a cryostatic ancillary apparatus. The spectral simulations were obtaind by the Bruker SimFonia or XEPR programmes.

The EPR pattern was always composed of a single feature. Its intensity *Y* was simulated as :

$$Y = A\frac{d}{dB}\left(\chi''+\alpha\chi'\right)+ sB + y_0 \qquad (1)$$

where *B* is the magnetic field, *A* and y_0 are scaling factors, *s* is the baseline slope, χ" and χ' are the imaginary (absorption) and the real (dispersion) components, respectively, of the complex magnetic susceptibility $\chi = \chi' - i\,\chi''$). $\alpha = tan\ \phi$ is the line-shape asymmetry parameter, where ϕ is the phase shift of the microwave magnetic field resulting from the electromagnetic shielding effect (*skin effect*) by conducting charge carriers. Therefore, $\alpha \neq 0$ is expected when the sample is characterized by electron conductivity only. In addition, the thickness *d* of the sample must be larger than its *skin depth* δ [33,34]. Keeping constant the microwave frequency, higher α values would indicate stronger *skin effect,* due to higher electron conductivity at the sample surface and/or to higher d/δ ratio.

2.3 – Catalytic activity and poisoning tests

Ca. 0.15 g of catalyst, pelletised, ground and sieved to 0.15-0.25 mm particles were loaded in a continuous quartz, 7mm i.d., vertical tubular reactor. The catalyst was activated in flowing air (20 cm^3/min) by increasing temperature up to 600°C (10°C/min), then kept for 1 h. The activity tests were carried out by feeding 30 cm^3/min (STP) of a gas mixture composed of 0.34 vol% CH_4, 33.3 vol% air, He balance, while increasing temperature by 10°C/min from 200°C up to 600°C. Gas flow rate was regulated by means of mass flowmeters (Brooks Instruments, mod. 5850) governed by a control unit (Brooks, mod. 0154). The outcoming gas was analysed in line by means of a quadrupolar mass spectrometer (MKS, PPT Residual Gas Analyzer), selecting proper mass fragments. Mass spectrometric (MS) data showed sometimes a small drift of the baseline, which led to

uncertain determination of T_0, *i.e.* the temperature at which methane conversion started. Therefore, this activity testing procedure was previously validated by analysing the effluent gas by gas-chromatography, the results of the two testing methods being comparable within ±10°C. The experimental error of MS activity tests has been calculated on the basis of 4 repeated analyses, by comparing the conversion values at 450°C, and resulted *ca*. 7%.

To better quantify the activity trend, the kinetic constant was also calculated (Table 4), by assuming a pseudo-first order reaction with respect to methane and pseudo-zero order with respect to oxygen, the latter being the excess reactant [19, 35]. If the kinetic investigation is carried out under over-stoichiometric conditions (O_2/CH_4>5) and in the conversion range between 20% and 80%, the kinetic constant may be calculated as [36]:

$$k_m\left[\frac{\mu mole}{s \cdot g \cdot atm}\right] = \frac{V \cdot 1000}{V_m \cdot 60 \cdot m \cdot P} \ln\left(\frac{1}{1-\alpha}\right)$$

where V is the volumetric flow rate (cm^3/min) of the gas mixture, V_m (L/mol) the molar volume, P the total pressure (atm), α the methane conversion fraction and m the mass of catalyst (g).

Catalyst poisoning [14,15] was done in the same apparatus at 450°C, by injecting 4 doses of 0.15 mg of tetrahydrothiophene (THT, Fluka, pur. >97%) per g of catalyst, each set of four injections being defined as “cycle” (1 cycle = 0.6 mg THT per g of catalyst). The catalytic activity was monitored *“in operando”* during poisoning, by continuously analysing the relevant mass fragments (CH_4, THT, SO_2, SO_3, CO, CO_2, H_2O) and plotting them as partial pressure *vs*. time. The data have been further elaborated to determine the transient response of the catalyst during poisoning, as better detailed in the following sections. A standard activity test was then repeated after every poisoning cycle, in order to measure the residual activity.

3 – RESULTS AND DISCUSSION

3.1 - Catalysts characterisation

A much lower SSA (Table 1) was obtained with the SG-prepared catalysts than with the FP ones, silver doping increasing the SSA in all cases. However, no clear relationship between SSA and silver loading was noticed.

According to the XRPD data, the main phase corresponds to rhombohedral (non-stoichiometric) $LaMnO_{3+\delta}$, characterised by a double reflection at $2\theta \approx 33°$ for SG samples, whereas the main phase corresponds to monoclinic $LaMnO_{3+\delta}$ for FP samples. Reflections of metallic silver ($2\theta \approx 38.1°$, 44.6° and 64.6°) were sometimes observed for the doped samples, with increasing intensity at high Ag loading, in line with the much lower solubility of Ag in the $LaMnO_3$ framework with respect to other dopants [37, 38]. The FP-prepared samples showed a small reflection of metallic silver even after 5% Ag loading, whereas it was almost undetectable for the SG prepared ones. An evident broadening of Bragg's peaks was also observed for FP samples due to nanostructuring. Regrettably, it was impossible to ascertain whether or not Ag_2O was present in the perovskite-structured samples, because the main Ag_2O (1 1 1) reflection ($2\theta \approx 33°$) perfectly overlaps the main reflection of the $LaMnO_3$ phase.

The Rietveld refinements carried out for the FP and SG samples are shown in Fig. 1 and 2, respectively, and the fitting results for all the samples are reported in Table 2.

At room temperature the FP samples belong to the monoclinic $P2_1/c$ space group [32]; conversely for SG samples a rhombohedral structural model, space group R-3c [32], was used to fit all the XRPD patterns. For the SG sample with x=0.10 also the metallic Ag phase has been considered in the refinement.

According to Mitchell *et al*. [32], the crystal structure of undoped and doped $LaMnO_3$ materials (at fixed temperature) is strictly connected to the Mn^{4+} concentration (hereinafter

[Mn^{4+}]) inside the lattice. In particular, the monoclinic distortion is observed for a full cation stoichiometry and for a formal valence state +3 of Mn cations. When rising [Mn^{4+}], transitions to the orthorhombic and then to the rhombohedral phases occur. As pointed out by Wold and Arnott [39] the synthesis conditions play an important role in defining the presence of Mn^{4+} in the $LaMnO_3$ lattice. FP is characterised by a flash calcination at high temperature (>1200°C) for a few milliseconds [40], a temperature level not achieved during the thermal treatment following the sol-gel synthesis (usually *ca*. 700-800°C). The high temperature and, perhaps, the rapid calcination of the FP method lead to the formation of an almost stoichiometric structure, where Mn mainly quenches in the +3 oxidation state. By contrast, a partial oxidation of Mn^{3+} to Mn^{4+} is favoured during the longer thermal treatment of the SG procedure.

Oxidation in these materials generally occurs through cation vacancies formation [41] and neutron powder investigations carried out on undoped and on Sr^{2+}-doped $LaMnO_3$ systems showed that cation vacancies are predominantly located at the La site [29]. Moreover, it should be noted that Mn^{4+} species can be also induced by substituting La^{3+} with lower valence ions [32]. The amount of Mn^{4+} species inside the lattice is therefore connected to the presence of La vacancies and to the Ag concentration index *x* in $La_{1-x}Ag_xMnO_3$ systems. The refined atomic site fractions related to La^{3+} as a function of *x* (Ag content) for SG samples is displayed in Fig. 3. When $x \geq 0.05$, the observed depletion of the La^{3+} atomic site fraction is clearly higher than the nominal values (dashed line). The amount of extraframework metallic Ag of the present SG catalysts is much lower (see Table 2) than that of previously reported (La,Ag)CoO_3 samples [15], indicating higher Ag solubility in the $LaMnO_3$ framework with respect to $LaCoO_3$. Hence, the substitution of Ag^+ for La^{3+} created greater amounts of Mn^{4+} ions in the $La_{1-x}Ag_xMnO_3$ structure and the La^{3+} atomic site fraction decreased with increasing *x* (Fig. 3). In addition, further information about the actual valence state of Mn ions can be obtained by unit cell volume values. As

reported by Rossmalen *et al*. [42] for $LaMnO_3$ undoped materials, the unit cell volumes decreases with increasing [Mn^{4+}]. By inspection of unit cell volume data as a function of *x* for $La_{1-x}Ag_xMnO_3$ SG samples (Table 2), a reduction of the unit cell volume values is evident for $x \geq 0.05$. This result confirms the increase of Mn^{4+} content with increasing *x* and, hence, the solubility of Ag ions in the $LaMnO_3$ crystal lattice. By contrast, no appreciable variation of the unit cell volume was observed for the monoclinic $La_{1-x}Ag_xMnO_3$ FP samples and, therefore, a valence state +3 prevailed for Mn cations.

EPR spectra confirmed the presence of higher Mn^{4+} amounts in the SG-prepared than in the FP-prepared catalysts. Further details can be added about this subject. Indeed, both crystal structure [32] and EPR intensity [10] are essentially connected to lattice [Mn^{4+}]. Therefore, the FP monoclinic structure, corresponding to an almost exact Mn^{3+} cation stoichiometry, is characterised by very faint EPR spectra, as expected. On the contrary, the (orthorhombic or rhombohedral) samples prepared by SG reveal more intense EPR spectra, hosting a greater amount of Mn^{4+} [32]. The presence of lattice Mn^{4+} is confirmed by the EPR line broadening with increasing temperature (Fig.4), due to electron jumping along the -Mn^{3+}-O-Mn^{4+}- chains, which form [11] in this mixed $Mn^{3+/4+}$ state (Double Exchange, DE [43]). Some contribution to the line-broadening observed with the FP materials could be attributed also to the greater amount of defects forming on the surface of solid particles, which are by far smaller than for the SG-prepared samples [12]. Narrowing of EPR lines in SG-prepared catalysts is due to faster DE, caused by the higher Mn^{4+} concentration, likely favoured by the thermal treatment, which lasts longer in the SG than in the FP procedure. $Ag^{1+/2+}$ substituting for La^{3+} causes further oxidation of some Mn^{3+} to Mn^{4+}, favouring the EPR (DE) line-narrowing with the FP-prepared samples (Fig.4). This was not observed with the SG-prepared materials, with which the EPR line-width likely had attained its smallest possible value even before that substitution. The great amount of $Ag^{1+/2+}$ substituting for La^{3+} in the lattice of SG prepared samples, though not

further affecting the EPR line-width at high temperature, has another consequence. It provides the sample of a great amount of conducting electrons, which favour the transition from paramagnetic to ferromagnetic resonance at T < 290 K (indirect magnetisation). This is revealed by the change of the symmetric, Lorentzian-shaped EPR line into a broad, asymmetric ferromagnetic resonance feature [44].

After catalytic use for CFC of FP samples, the EPR line-width decreased, approaching that of the analogous SG-prepared sample. Furthermore, it broadened with decreasing temperature at T < 290 K, in perfect analogy with the SG samples (Fig. 4 and 5). At last, the comparison between fresh, preactivated (in air at 600°C for 1 h) and aged samples (after catalytic use) evidenced that both the line-narrowing at T > 290 K and the formation of ferromagnetic domains at low temperature were not due to the catalytic use, but to the activation treatment in air.

In the present investigation, a α = 0 (see eq. (1)) value was found for the SG-prepared materials (*i.e.*, the EPR line was Lorentzian-shaped), whilst small $\alpha \neq 0$ values were found with the FP-prepared samples, the highest value ($\cong$ 0.054$\pm$0.002) being attained when doping a FP-prepared catalyst with Ag ($x \cong 0.10$). Positive α values are compatible with a *skin effect* due to the presence, on the sample surface, of Ag particles undissolved in the lattice, in agreement with the XRPD data, providing this sample of a low surface electron conductivity. In principle, also the conduction electrons of the surface Ag^0 particles could reveal an EPR line (adding to that of Mn^{4+}). However, that pattern is not detectable at temperatures higher than 77 K [45].

3.2 – Catalytic activity

Activity data are reported in Fig. 6 and summarised in Table 3 as the temperature (T_{50}) at which 50% conversion of methane was attained. In addition, the conversion at

450°C was reported in the same Table 3, to directly compare catalyst behaviour before and after poisoning by THT (*vide infra*).

Almost all the catalysts exhibited a very high activity, attaining full methane conversion below 600°C, with carbon dioxide + water as the only detected products. The SG-prepared $LaMnO_3$ catalyst represented an exception, allowing a maximum 65% methane conversion at 600°C.

The calculated kinetic parameters are also reported in Table 4. The activity of FP-prepared catalyst was always higher than that of SG-prepared ones with identical nominal composition. SSA is usually a less important parameters for this reaction when carried out in the *intrafacial* regime, where oxygen mobility through the lattice can represent the rate determining step. However, the higher is SSA, the lower is the crystal size of the powder and then the shorter is the pathway for oxygen from the bulk to the surface and *viceversa*, leading to a faster oxygen exchange between the surface and the bulk, given an equal total oxygen content.

Partial substitution of Ag for La led to increasing activity both for SG- and FP-prepared catalysts and the catalytic activity increased with increasing Ag substitution. This was more evident for the FP-prepared samples, which showed an almost doubling of the kinetic constant upon substitution of 10% Ag for La (Table 4). These data present an interesting difference with respect to our previous results on $La_{1-x}Ag_xCoO_3$ systems [15]. Indeed, in that case the insertion of silver into the cobaltite lattice did not lead to a significant improvement of activity. Particularly, for some catalysts the partial substitution of La by a so low valence ion dropped the reducibility of Co, which in turn led to a slower redox cycle and to a decrease of catalytic activity. An improvement of activity was achieved only when metallic Ag was substantially present in extra-framework position in relatively large particle size, therefore showing its own catalytic activity.

This latter point was checked by preparing two comparative samples by impregnation of Ag on the undoped $LaMnO_3$ samples, so leading to well detectable extralattice metallic isles (Fig 7), at difference with patterns reported in Fig. 1 and 2. Based on XRD patterns of Fig.7, the average Ag crystal size D (nm) was calculated with the Scherrer equation $D = \frac{0.9 \cdot \lambda \cdot 180}{B \cdot \cos\theta \cdot \pi \cdot 10}$, where λ (Å) the wavelength of the X-ray emitter, $B = \sqrt{FWHM^2 - 0.25^2}$, FWHM is the full reflection width at half maximum. The peak at $2\theta \approx 37°$ was chosen as reference. For the FP-$LaMnO_3$ supported sample D≈20nm, whereas for the SG-$LaMnO_3$ supported one D≈50nm, in line with the decreasing surface area of the support.

From the data reported in Tables 3 and 4 one may conclude that big Ag particles effectively improve the catalytic performance, but the effect is less positive than when at least part of Ag is inserted into the framework. This is particularly evident for the SG prepared samples, which experience only a doubling of methane conversion upon impregnation, much more upon intraframework substitution.

For all the present $La_{1-x}Ag_xMnO_3$ samples, the TPR profiles were characterised by two main peaks (Fig. 8*a*). The former, at low temperature, can be mainly attributed to the reduction of Mn^{4+} to Mn^{3+} and, if applicable, to Ag^+ reduction to Ag^0. By contrast the latter, at higher temperature, reveals the reduction of Mn^{3+} to Mn^{2+} with a possible partial decomposition of the perovskite structure. Unfortunately, a reliable quantification of H_2 uptake and most of all the determination of oxygen non-stoichiometry following the method reported in [46] was not possible for the present samples. Indeed, on one hand mass-spectrometric data are poorly suitable for quantification when the comparison between different analyses is concerned. In addition, the high temperature reduction feature did not completed in the temperature range allowed by our apparatus. Nevertheless, peak

deconvolution was attempted by Gaussian fitting for the first reduction peak when multiple contributions were observed.

Partial substitution of Ag^{+} for La^{3+} led to a decrease of the onset temperature of the first reduction peak and enlarged the reducibility range of Mn ions. A similar and more evident result was achieved for the samples prepared by impregnation. In some cases peak splitting was observed. The most evident case was represented by sample SG-$La_{0.9}Ag_{0.1}MnO_3$. Peak deconvolution evidenced the presence of three peaks, centred at ca. 220, 290 and 750°C (Fig. 8*b*). By comparing their integrated area one may conclude that the first represents *ca*. 8% of the second one. This may be correlated with dopant concentration and could be tentatively attributed to Ag^{+} reduction.

It was suggested [47,48] that doping with ions of the copper group (Cu, Ag, Au) leads to a weakening of the metal–oxygen bonds in the perovskite-like oxide. In the present case it may be expected that silver facilitates the pulling out of oxygen from the crystal lattice of the oxides in a similar way. The structural defects, *i.e.* oxygen vacancies, conferred by silver may also increase oxygen mobility through the bulk. The migration of lattice oxygen to extraframework metallic silver becomes also easier, thanks to the weakening of the interaction between oxygen and manganese ions. The release of oxygen from silver oxides (reduction at a relatively low temperature and even spontaneous thermal decomposition) is easier than in the case of manganese oxide compounds. Then the sequence of events — weakening of the Mn–O bonds, increased lattice oxygen mobility and its migration to silver — results in the lowering of the temperature of the first stage of reduction of the doped catalysts. Of course, this is possible only after the insertion of silver ions into the perovskite structure. A higher solubility of the dopant in the manganite framework with respect to the cobaltite can be deduced by comparing the present data with those previously published for $La_{1-x}Ag_xCoO_3$ systems [15]. This is supported also by both XRPD and EPR present data. This limits the catalytic effect of extraframework

metallic Ag in the present case. The attention must be here better focused on the effect of lattice Ag ions on Mn reducibility and oxygen mobility. The higher Mn^{4+} reducibility, witnessed by TPR analysis, improved catalytic activity and the growing Mn^{4+} reduction with higher Ag loading showed beneficial to oxygen mobility. This was particularly relevant for the nanosized FP samples, for which a shorter bulk-surface path is present (*vide supra*). The latter feature favours methane oxidation by increasing the availability of bulk oxygen and easing catalyst reoxidation in the second step of the Mars van Krevelen mechanism.

Finally, it should be noticed that the present FP-prepared $La_{0.9}Ag_{0.1}MnO_{3\pm\delta}$ catalyst showed the most active for methane CFC among the wide series of cobaltite and manganite perovskites prepared and tested for this application [14, 15].

3.3 Resistance to sulphur poisoning

A detailed description of the testing procedure has been given elsewhere [14]. A preliminary set of experiments allowed concluding that THT instantly oxidises to SO_2, CO_2 and H_2O in the presence of the catalyst at the selected poisoning temperature (450°C). This temperature has been chosen because most samples exhibit the highest reaction rate around this value and the conversion *vs*. temperature curve is very steep, so better highlighting the effect of poisoning [14].

Under the conditions of methane combustion, SO_2 forming during the oxidation of sulphur-containing substrates may adsorb on catalyst surface. Consequently, the amount of active sites decreases and catalytic activity lowers. Adsorbed sulphur-containing species can react with surface oxygen with formation of SO_2^- and SO_3^- radicals. Once formed, these species can react also with gaseous oxygen with formation of SO_4^-.,All these sulphur species can decompose or desorb from the surface [49], depending on temperature. In addition, they can react with the metal ions of the perovskite lattice,

leading to partial or total decomposition of the structure, with change of the cell parameters [50].

The Rietveld refinements relative to poisoned SG $LaMnO_3$ and poisoned FP $La_{0.95}Ag_{0.05}MnO_3$ are shown in Fig. 9. The structural model of the former converged through the refinement of the structural parameters related to three different phases: (*i*) rhombohedral $LaMnO_3$ (space group R-3c); (*ii*) tetragonal Mn_3O_4 (space group *I* 4_1/*amd*) ; (*iii*) hexagonal $La_2O_2CO_3$ (space group *P*6_3/*mmc*). The refined weight fractions (%) of the three phases were 66.89(25)%, 7.33(25)%, 25.78(27)%, respectively. It is worth noticing that the formation of the $La_2O_2CO_3$ phase occurs quite likely during catalyst use. In fact the reported synthesis conditions for the $La_2O_2CO_3$ phase (T=530-550°C in air [51]) are not very different from those of poisoning, when feeding a gas mixture of CH_4 and air at T=450°C. .

Contrary to the structural decomposition observed with poisoned SG catalyst, a single $LaMnO_3$ rhombohedral phase (space group R-3c) was sufficient to fit the XRPD pattern of poisoned FP $La_{0.95}Ag_{0.05}MnO_3$. No trace of other phases was found, at least within the detection limit of the technique. It should be also underlined that no extensive sintering of the spent FP catalyst could be inferred from XRPD analysis (Fig.9).

The high temperature attained in the flame, followed by a rapid quenching, freezes the stable monoclinic phase of the FP samples (Fig.1). In that phase, Mn ions are present almost exclusively in the 3+ oxidation state, unfavouring both a high concentration of Mn^{4+} ions (Fig.8a) and a large dissolution of Ag ions in the lattice (*vide supra*). During activation and catalytic reaction, the monoclinic phase shifts to a rhombohedral one, stable even after several poisoning cycles (Fig.9). Therefore, the better resistance to structural decomposition upon sulphur poisoning of FP samples, with respect to SG ones, could be connected with the higher thermal resistance of the former, conferred by the FP

preparation procedure, preventing extensive structural reorganisation upon heating in a possibly reactive atmosphere (SO_2).

All samples lost part of their initial activity after poisoning, but the activity scale remained unchanged (*vide supra*). The activity curves after poisoning are presented in Fig. 10 and residual activity is summarised in Table 3. Ag insertion did not change appreciably the resistance to poisoning for the FP prepared samples, methane conversion decreasing by *ca*. 8-9 points % as for the Ag-free sample. However, when considering the relative residual conversion (RRC in Table 3) of all the FP samples, one may conclude that at least 85% of the initial activity was retained after poisoning, growing up to 88-89% for the Ag-doped samples. On the other hand, a higher absolute drop of conversion was visible for the SG-prepared Ag-doped with respect to the undoped sample. Nevertheless, the residual activity after poisoning was less than 30% of the initial value (Table 3), due to the very poor catalytic performance of SG-$LaMnO_3$.

As already mentioned, silver doping changed the lattice parameters and the properties of the perovskite, but its effect on the resistance to sulphur poisoning is controversial. On one hand, the difference of valence state between La and Ag brings part of Mn^{3+} to its higher valence state, namely to Mn^{4+}, which is more acidic and weakens the interaction between SO_2 and the surface. On the other hand, framework Ag ions substitution increases the amount of oxygen vacancies, as in the case of Co-based perovskites [15], that in turn makes easier the SO_2 adsorption. It should be also mentioned that extraframework metallic silver may directly act as a sulphur guard, by reacting more promptly with sulphur compounds than the main perovskite-like phase. The latter effect showed less sensitive for the present catalysts with respect to the previously reported (La,Ag)CoO_3 samples, due to the mentioned higher solubility of Ag in the manganite structure than in the cobaltite one [15]. However, it may explain why the FP-prepared samples showed much more resistant to sulphur poisoning than the SG ones. Indeed,

based on the above reported structural considerations, the same crystal phase is reached for the FP and SG samples upon activation in air, allowing the allocation of Mn^{4+}. This would in principle lead to similar resistance to poisoning, due to the mentioned acidic character of the latter ion.

The partial oxidation of Mn^{3+} to Mn^{4+} helped improving the resistance to poisoning for the SG-prepared samples with low Ag loading, in which silver was mainly in lattice position. FP-prepared catalysts, even with a low substitution level, were characterised by a lower Ag incorporation into the lattice with respect to the SG samples. Extraframework silver exploits its beneficial effect as sulphur guard rather than as activity enhancer, since Ag^0 particle size was too small from that point of view [15]. It is worth mentioning that a satisfactory residual activity after poisoning has been achieved in comparison with the undoped sample, also thanks to the catalytic activity improvement of the fresh catalyst upon Ag-doping. Indeed, the FP-$La_{0.9}Ag_{0.1}MnO_3$ sample was still able to convert 75% of methane at 450°C after four poisoning cycles, which is a catalytic performance much better even than that of the fresh FP-$LaMnO_3$ sample.

At last, a regeneration test was attempted for sample $La_{0.9}Ag_{0.1}MnO_3$, by heating the sample in H_2 flow at 500°C for 1 h, followed by oxidation in air at 600°C for 1 h. This treatment showed effective for some manganite and cobaltite samples doped with Pt or Pd [14]. Unfortunately, in the present case the regeneration procedure kept the conversion unchanged.

From the point of view of protection against poisoning, silver showed less effective than Sr^{2+}, since no decrease of conversion has been observed with lanthanum manganites doped with Sr [14]. With the present Ag-doped catalysts the main advantage is the improvement of initial activity, which leads to satisfactory results even after poisoning.

3.4 Transient response during poisoning

From the point of view of the poisoning mechanism, we recently introduced a semiquantitative evaluation of the transient response of the catalysts [14]. A typical pattern of CH_4 partial pressure *vs*. time is reported in Fig. 11, showing its evolution during THT injections (vertical lines represent injection time). Two parameters are used to characterise this curve [14, 15]. Indeed, for each poisoning cycle (injection) we calculated the slope of the tangent of the p_{CH4} *vs*. time curve in the starting point of each cycle (angle β in Fig. 11). This parameter may be considered as an initial poisoning rate. Then, by approximating the whole curve with a straight line, its slope (angle α in Fig. 11) has been interpreted as an average poisoning rate. The results are presented in Tables 5 and 6. From these data we may tendentially infer that Ag doping decreased both such parameters. Furthermore, when comparing the initial and average poisoning rates for every catalyst, one may notice that the former is usually higher than or comparable to the latter. This is an interesting information since the shape of the curve indicate how fast the catalytic system answers to the transient poisoning and if it tends towards a stabilisation or not. For example, catalysts with a steep curve should be regarded as better, that trend meaning quick answer to the poison followed by a rapid stabilisation.

The poisoning profiles of the present catalysts were often characterised by a linear variation of methane partial pressure (approximately equal initial and average poisoning rates). Furthermore, the deactivation rate during the first cycles was usually higher than for the last one, evidencing that SO_2 adsorption was quick on particularly active sorption sites, progressively saturated (decreasing poisoning rate). By comparing the average and the initial poisoning rates, one may notice the positive tendency towards stabilisation and a fast response of the catalyst. Finally, the addition of 10% Ag strongly improved resistance for both catalyst series, since an evident decrease of the average poisoning rate was observed, though keeping a fast initial response.

4 – CONCLUSIONS

Ag-doped $LaMnO_3$ samples prepared by FP and SG have been compared as catalysts for the CFC of methane.

XRPD and EPR characterisation revealed that the (orthorhombic or rhombohedral) freshly SG-prepared materials possess a higher capability of hosting both $Ag^{1+/2+}$ and Mn^{4+} ions with respect to the FP-prepared ones. Therefore, a higher catalytic activity should be expected with them from this point of view. Furthermore, the higher SSA of the FP-prepared samples should not favour as such their catalytic activity for the CFC of methane, because this reaction occurs in the *intrafacial* regime, where oxygen mobility through the lattice can represent the key factor. However, all the FP-prepared catalysts showed much more active with respect to the corresponding SG ones. This can be explained on the basis of three considerations. The first is that the activation process of the FP-prepared samples causes a transition of phase from monoclinic to orthorhombic (or rhombohedral) structure, similar to that of the SG-prepared materials. The second consideration is that by keeping fixed the total oxygen content of the sample, the higher is SSA, the lower is the crystal size of the powder and the shorter is the pathway for oxygen from the bulk to the surface and *viceversa*, leading to higher oxygen availability and faster reoxidation of the catalyst. Finally, if big extralattice Ag particles can form they may strongly improve catalytic activity as in the case of samples prepared by impregnation.

At last, we must outline that the addition of Ag led to an increased Mn^{n+} reducibility and oxygen mobility through the lattice of both SG- and FP-prepared catalysts and, hence, to an increase of activity with respect to the undoped samples.

Silver improved also the resistance to sulphur poisoning, mainly by increasing the concentration of the acidic Mn^{4+} ions and weakening the SO_2 adsorption on the catalyst.

REFERENCES

1. H. Chiba, M. Kikuchi, K. Kusaba, Y. Miraoka, Y. Syono. Solid State Commun. 99 (1966) 499.
2. A. Urushibara, Y. Moritomo, T. Arima, A. Asamitsu, G. Kido, Y. Tokura. Phys. Rev. B 51 (1995) 14103.
3. Y. Tokura, A. Urushibara, Y. Moritomo, T. Arima, A. Asamitsu, G. Kido, N. Furukawa. J. Phys. Soc. Jpn 63 (1994) 3931.
4. B. Doudin, J-Ph Ansermet. Europhys. News 28 (1997) 14.
5. C.Rettori, D. Rao, J.Singley, D. Kidwell, S.B. Oseroff, M.T. Causa, J.J. Newmeier, K.J. McClellan, S-W. Cheong, S. Schultz. Phys. Rev. B 55 (1997) 3083.
6. S.B. Oseroff, M. Torikachvili, J. Singley, S. Ali. Phys. Rev. B 1996 (53) 6521.
7. M.S. Seehra, M.M. Ibrahim, V.S. Babu, G. Srinivasan. J. Phys. Condens. Matter 8 (1996) 11283.
8. N. Furukawa. J. Phys. Soc. Jpn. 65 (1996) 1174.
9. G. Papavassiliou, M. Fardis, M. Milia, A. Simopoulos, G. Kallias, M. Pissas, D. Niarchos, N. Ioannidis, C. Dimitropoulos, J. Dilinsek. Phys. Rev. B 55 (1997) 15000.
10. A.Shengelaya, Guo-meng Zhao, H.Keller, K.A.Muller. Phys.Rev.Lett. 77 (1996) 5296.
11. C. Oliva, L. Forni, P. Pasqualin, A. D'Ambrosio, A.V. Vishniakov. Phys. Chem. Chem. Phys. 1 (1999) 355.
12. C. Oliva, L. Forni. Catalysis Commun. 1 (2000) 5.
13. G.L. Chiarello, I. Rossetti, L. Forni, J. Catal., 236 (2005) 251.
14. I. Rossetti, O. Buchneva, C. Biffi, R. Rizza, Appl. Catal. B: Environmental, 89 (2009) 383.
15. O. Buchneva, I. Rossetti, C. Biffi, M. Allieta, A. Kryukov, N. Lebedeva, Appl. Catal. A 370 (2009) 24.

16. T. Nakamura, M. Misono, Y. Yoneda, J. Catal. 83 (1983) 151.
17. T. Nakamura, M. Misono, Y. Yoneda, Bull. Chem. Soc. Jpn 55 (1982) 394.
18. S. Ponce, M. A. Peña, J. L. G. Fierro, Appl. Catal. B 24 (2000) 193.
19. H. Arai, T. Yamada, K. Eguchi, T. Seiyama, Appl. Catal., 26 (1986) 265.
20. L.Fabbrini, A.Kryukov, S.Cappelli, G.L.Chiarello, I.Rossetti, C.Oliva, L. Forni, J. Catal., 232(2) (2005) 247.
21. N. Hien, N.P. Thuy, Physica 319 (2002) 168.
22. S.L. Ye,W.H. Song, J.M. Dai, K.Y.Wang, S.G.Wang, C.L. Zhang, J.J. Du, Y.P. Sun, J. Fang, J. Magn. Mater. 248 (2002) 26.
23. M. Battabyal, T.K. Dey, Solid State Commun. 131 (2004) 337.
24. X.E. Verykios, F.P. Stein, R.W. Coughlin, Catal. Rev.-Sci. Eng., 22 (1980) 197.
25. H.A. Engelhardt, D. Menzel, Surf. Sci., 57 (1976) 591.
26. K.C. Prince, A.M. Bradshaw, Surf. Sci. 126 (1983) 49.
27. K.L. Anderson, J.K. Plischke, M.A. Vannice, J. Catal., 128 (1991) 148.
28. L. Kundakovic, M. Flytzani-Stephanopoulos, Appl. Catal. A: General, 183 (1999) 35.
29. Selected Powder Diffraction Data, Miner. DBM (1-40), J.C.P.D.S., Swarthmore, PA, 1974-1992.
30. A.C. Larson, R.B. Von Dreele. Los Alamos National Laboratori Report LAUR 86 (2004) 748.
31. B. H. Toby, J. Appl. Cryst. 34 (2001) 210.
32. J.F. Mitchell, D.N. Argyriou, C.D. Potter, D.G. Hinks, J.D. Jorgensen, S.D. Bader. Phys. Rev. B 54 (1996) 6172..
33. F.J. Dys G. Feher, A.F. Kip, Phys. Rev. 98 (1955) 337.
34. G. Feher, A.F. Kip, Phys. Rev. 98 (1955) 337.
35. M.A. Peña, J.L.G. Fierro. Chem. Rev., 101 (2001) 1981.

36. C. Batiot-Dupeyrat, F. Martinez-Ortega, M. Ganne, J.M. Tatibouët, Appl. Catal. A: General, 206 (2001) 205.
37. A. Machocki, T. Ioannides, B. Stasinska, W. Gac, G. Avgouropoulos, D. Delimaris, W. Grzegorczyk, S. Pasieczna, J. Catal., 227 (2004) 282.
38. B. Kucharczyk, W. Tylus, Appl. Catal. A: General, 335 (2008) 28.
39. A. Wold and R. J. Arnott, J. Phys. Chem. Solids 9 (1959) 176.
40. G.L. Chiarello, I. Rossetti, P. Lopinto, G. Migliavacca, L. Forni. Catal. Today, 117 (2006) 549.
41. J. Töpfer and J. B. Goodenough. J. Solid State Chem. 130 (1997) 117.
42. J.A.M. van Roosmalen, P. van Vlaanderen, E.H.P. Cordfunke, W.L. Ijdo, D.J.W. Ijdo. J. Sol. State Chem. 114 (1995) 516.
43. C. Zener, Phys.Rev., 82 (1951) 403.
44. L. Bonneviot, D.Olivier “Ferromagnetic Resonance” in “Catalyst Characterization. Physical Techniques sor Solid Materials”, B.Imelik and J.C.Vedrine, Eds., Plenum Press, 1994.
45. R. Monot, C. Narbel, J.-P. Borel, Nuovo Cimento, 19 (1974) 253.
46. I. Rossetti, C. Biffi, L. Forni, Chem. Eng. J., DOI: 10.1016/j.cej.2010.06.003
47. S. Minico, S. Scire, C. Crisafulli, R. Maggiore, S. Galvango, Appl. Catal. B 28 (2000) 245.
48. S. Scire, S. Minico, C. Crisafulli, S. Galvango, Catal. Commun. 2 (2001) 229.
49. Lowell P.S., K. Schwitzgebel, T.B. Parsons, K.S. Sladek, Ind. Eng. Chem. Proc. Des. Develop. 10 (1971) 384.
50. L. Wan in: .G. Tejuca, J.L.G. Fierro (Eds.), Properties and applications of the Perovskite-type oxides, Marcel Dekker, Mew York, 1993, p. 145.
51. J. P. Attfield, G. Férey, J. Solid State Chem. 82 (1989) 132.

TABLES

Table 1. Samples composition and BET specific surface area (SSA). T_{red} = onset of the first reduction peak from TPR analysis.

Sample	Method	SSA, m^2/g	T_{red} (°C)
$LaMnO_3$	FP	56	420
$LaMnO_3$	SG	8	460
$La_{0.95}Ag_{0.05}MnO_3$	FP	251	-
$La_{0.95}Ag_{0.05}MnO_3$	SG	27	-
$La_{0.9}Ag_{0.1}MnO_3$	FP	103	310
$La_{0.9}Ag_{0.1}MnO_3$	SG	22	290
10%Ag+$LaMnO_3$*	FP	32	250
10%Ag+$LaMnO_3$*	SG	7	270

* Ag loaded by wet impregnation with $AgNO_3$ of the undoped sample.

Table 2. Room-temperature structural parameters for $La_{1-x}Ag_xMnO_3$ (with x=0, 0.05, 0.1) FP and SG samples. The refined atomic site fractions (ASF) related to La^{3+} for SG samples and the agreement factors R_p(%) between observed and calculated are also listed.

Synthesis Technique	FP	SG	FP	SG	FP	SG
x Ag content	0.0	0.0	0.05	0.05	0.10	0.10
Space Group	$P2_1/c$	$R\bar{3}c$	$P2_1/c$	$R\bar{3}c$	$P2_1/c$	$R\bar{3}c$
a(Å)	7.925(3)	5.5078(5)	7.936(6)	5.4741(8)	7.916(7)	5.4774(6)
b(Å)	7.759(1)	5.5078(5)	7.749(2)	5.4741(8)	7.755(2)	5.4774(6)
c(Å)	7.895(2)	13.355(2)	7.894(4)	13.332(3)	7.891(4)	13.326(2)
β (°)	91.46(1)	-	91.80(3)	-	91.67(3)	-
V(Å^3)	485.3(2)	350.8(8)	485.2(4)	345.9(1)	484.7(4)	346.2(1)
La^{3+} ASF	-	1.010(5)	-	0.825(6)	-	0.794(5)
Rp(%)	9.86	9.21	12.36	13.43	12.42	12.17

Table 3. Activity data of fresh and poisoned catalysts, *i.e*. after the addition of 0.6 (1st cycle) and 2.4 (last cycle) mg of THT/g of catalyst. T_0 = temperature at which CH_4 conversion started; T_{50} = temperature of 50% CH_4 conversion; $Conv_{450°C}$ = CH_4 % conversion at 450°C. Activity data for poisoned samples given as residual CH_4 % conversion at 450°C. Δ = activity loss due to poisoning (conversion of fresh sample – residual conversion after the last poisoning cycle) expressed in points %. RRC = Relative residual conversion, *i.e.* fraction of the conversion of the fresh catalyst retained after poisoning.

Sample	Method	Fresh catalyst		Poisoned catalyst		Δ, %	RRC
		T_{50}	$Conv_{450}$,%	I cycle, $Conv_{450}$, %	Last cycle, $Conv_{450}$, %		
$LaMnO_3$	FP	435	59.0	54.1	49.9	9.1	0.85
$LaMnO_3$	SG	583	7.5	4.0	2.0	5.5	0.27
$La_{0.95}Ag_{0.05}MnO_3$	FP	427	66.0	60.5	58.0	8.0	0.88
$La_{0.95}Ag_{0.05}MnO_3$	SG	479	36.3	27.5	17.0	19.3	0.47
$La_{0.9}Ag_{0.1}MnO_3$	FP	395	84.0	82.0	75.0*	9.0	0.89
$La_{0.9}Ag_{0.1}MnO_3$	SG	464	43.6	30.1	22.1	21.5	0.51
10%Ag+$LaMnO_3$	FP	400	80	76	65	15	0.81
10%Ag+$LaMnO_3$	SG	570	13.5	12.5	5	8.5	0.37

* After regeneration in H_2 [14] this value was ca. 74 %.

Table 4. Kinetic constant of methane combustion at 450°C.

Sample	Method	$k_m^{450}, \frac{\mu mole}{s \cdot g \cdot atm}$
$LaMnO_3$	FP	154
$LaMnO_3$	SG	n.d.*
$La_{0.95}Ag_{0.05}MnO_3$	FP	187
$La_{0.95}Ag_{0.05}MnO_3$	SG	77
$La_{0.9}Ag_{0.1}MnO_3$	FP	272
$La_{0.9}Ag_{0.1}MnO_3$	SG	96
10%Ag+$LaMnO_3$	FP	238
10%Ag+$LaMnO_3$	SG	n.d.*

* n.d. = not determined since this catalysts did not reach 20% methane conversion at 450°C.

Table 5. Average deactivation rate (x 10^{-4} Torr/min; 1 Torr = 133 Pa) during each poisoning cycle (Fig. 11, slope of angle α).

Sample	Method	I cycle	II cycle	III cycle	IV cycle
$LaMnO_3$	FP	14	200	200	16
$LaMnO_3$	SG	78	130	9	24
$La_{0.95}Ag_{0.05}MnO_3$	FP	130	220	170	130
$La_{0.95}Ag_{0.05}MnO_3$	SG	15	0	310	0
$La_{0.9}Ag_{0.1}MnO_3$	FP	38	50	0	17
$La_{0.9}Ag_{0.1}MnO_3$	SG	35	30	0	47
10%Ag+$LaMnO_3$	FP	200	0	0	0
10%Ag+$LaMnO_3$	SG	13	0	0	6

Table 6: Initial deactivation rate (x 10^{-4} Torr/min; 1 Torr = 133 Pa) for each poisoning cycle (Fig. 11, slope of angle β).

Sample	Method	I cycle	II cycle	III cycle	IV cycle
$LaMnO_3$	FP	100	200	200	0
$LaMnO_3$	SG	200	200	0	70
$La_{0.95}Ag_{0.05}MnO_3$	FP	80	400	320	200
$La_{0.95}Ag_{0.05}MnO_3$	SG	0	0	60	0
$La_{0.9}Ag_{0.1}MnO_3$	FP	0	100	0	100
$La_{0.9}Ag_{0.1}MnO_3$	SG	200	100	0	100
10%Ag+$LaMnO_3$	FP	500	0	0	0
10%Ag+$LaMnO_3$	SG	30	0	200	150

FIGURE CAPTIONS

Fig.1: Observed (crosses) and calculated (continuous line) XRPD patterns for (a) $LaMnO_3$, (b) $La_{0.95}Ag_{0.05}MnO_3$, (c) $La_{0.9}Ag_{0.1}MnO_3$ FP samples (as prepared). The difference between the observed and calculated patterns is displayed at the bottom of each panel (dotted line).

Fig.2: Observed (crosses) and calculated (continuous line) XRPD patterns for (a) $LaMnO_3$, (b) $La_{0.95}Ag_{0.05}MnO_3$, (c) $La_{0.9}Ag_{0.1}MnO_3$ SG samples (as prepared). The difference between the observed and calculated patterns is displayed at the bottom of each panel (dotted line). The marker (*) in panels (a) and (c) indicates an unknown impurity.

Fig.3: Refined atomic site fractions related to La^{3+} as a function of *x* (Ag mole fraction) for SG samples (black dots). The nominal atomic site fraction values as a function of *x* for the same cation are also shown (dashed line).

Fig. 4: EPR spectra linewidth *vs*. Temperature. (■) SG-$LaMnO_3$, (▲) SG-$La_{0.95}Ag_{0.05}MnO_3$, (♦) SG-$La_{0.9}Ag_{0.1}MnO_3$, (□) FP-$LaMnO_3$, (△) FP-$La_{0.95}Ag_{0.05}MnO_3$, (◊) FP-$La_{0.9}Ag_{0.1}MnO_3$.

Fig.5: EPR spectral intensity (arbitrary units) of representative samples. *a)* SG-$La_{0.95}Ag_{0.05}MnO_3$: (■) at 250K, (▲) at 320K, (♦) at 400K. *b)* FP-$La_{0.95}Ag_{0.05}MnO_3$ after catalytic use, (■) at 250K, (▲) at 320K, (♦) at 400K.

Fig. 6: Catalytic activity of fresh catalysts (■) SG-$LaMnO_3$, (▲) SG-$La_{0.95}Ag_{0.05}MnO_3$, (♦) SG-$La_{0.9}Ag_{0.1}MnO_3$, (□) FP-$LaMnO_3$, (△) FP-$La_{0.95}Ag_{0.05}MnO_3$, (◊) FP-$La_{0.9}Ag_{0.1}MnO_3$. Operating conditions: CH_4 = 0.34 vol%, air = 33.3 vol%, He balance; total flow rate = 30 cm^3/min (STP); mass of catalyst = 0.15 g; heating rate = 10 °C/min.

Fig. 7: XRPD patterns of fresh 1) FP 10%AG+$LaMnO_3$, 2) SG 10%Ag+$LaMnO_3$.

Fig 8: a) Temperature-Programmed Reduction (TPR) pattern of selected samples: SG-$LaMnO_3$ (solid black line), SG-$La_{0.9}Ag_{0.1}MnO_3$ (dotted black line), FP-$LaMnO_3$ (solid grey line) and FP-$La_{0.9}Ag_{0.1}MnO_3$ (dotted grey line); b) example of peak deconvolution for sample SG-$La_{0.9}Ag_{0.1}MnO_3$. Operating conditions: H_2 = 10 vol% in He; total flow rate = 40 cm^3/min (STP); mass of catalyst = 0.15 g; heating rate = 10 °C/min. Signal collection by mass spectrometry.

Fig. 9: Observed (crosses) and calculated (continuous line) XRPD patterns for poisoned samples (a) SG-$LaMnO_3$, (b) FP-$La_{0.95}Ag_{0.05}MnO_3$. The difference between the observed and calculated patterns is displayed at the bottom of each panel (dotted line). The agreement factors are R_p=11.11% and R_p=8.26% for (a) and (b) respectively.

Fig. 10: Catalytic activity after sulphur poisoning of SG samples (after the addition of 2.4 mg THT/g of catalyst): (■) SG-$LaMnO_3$, (▲) SG-$La_{0.95}Ag_{0.05}MnO_3$, (♦) SG-$La_{0.9}Ag_{0.1}MnO_3$, (□) FP-$LaMnO_3$, (△) FP-$La_{0.95}Ag_{0.05}MnO_3$, (◊) FP-$La_{0.9}Ag_{0.1}MnO_3$.

Fig. 11: Evolution of the CH_4 MS-signal during poisoning at 450°C for FP-$La_{0.95}Ag_{0.05}MnO_3$. The values of α and β, representing the average and initial poisoning rates are reported in Tables 5 and 6.

Fig. 1

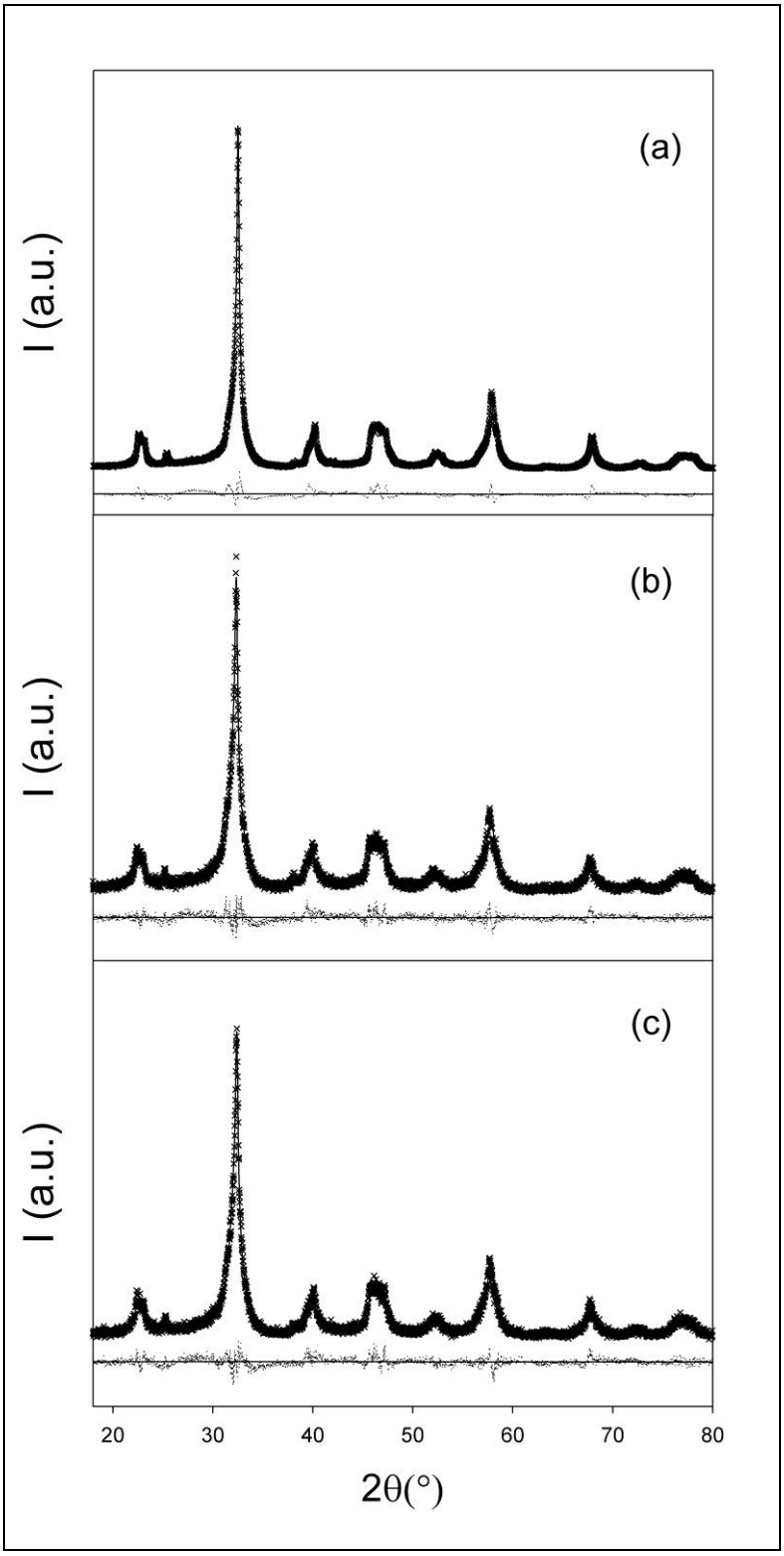

Fig. 2

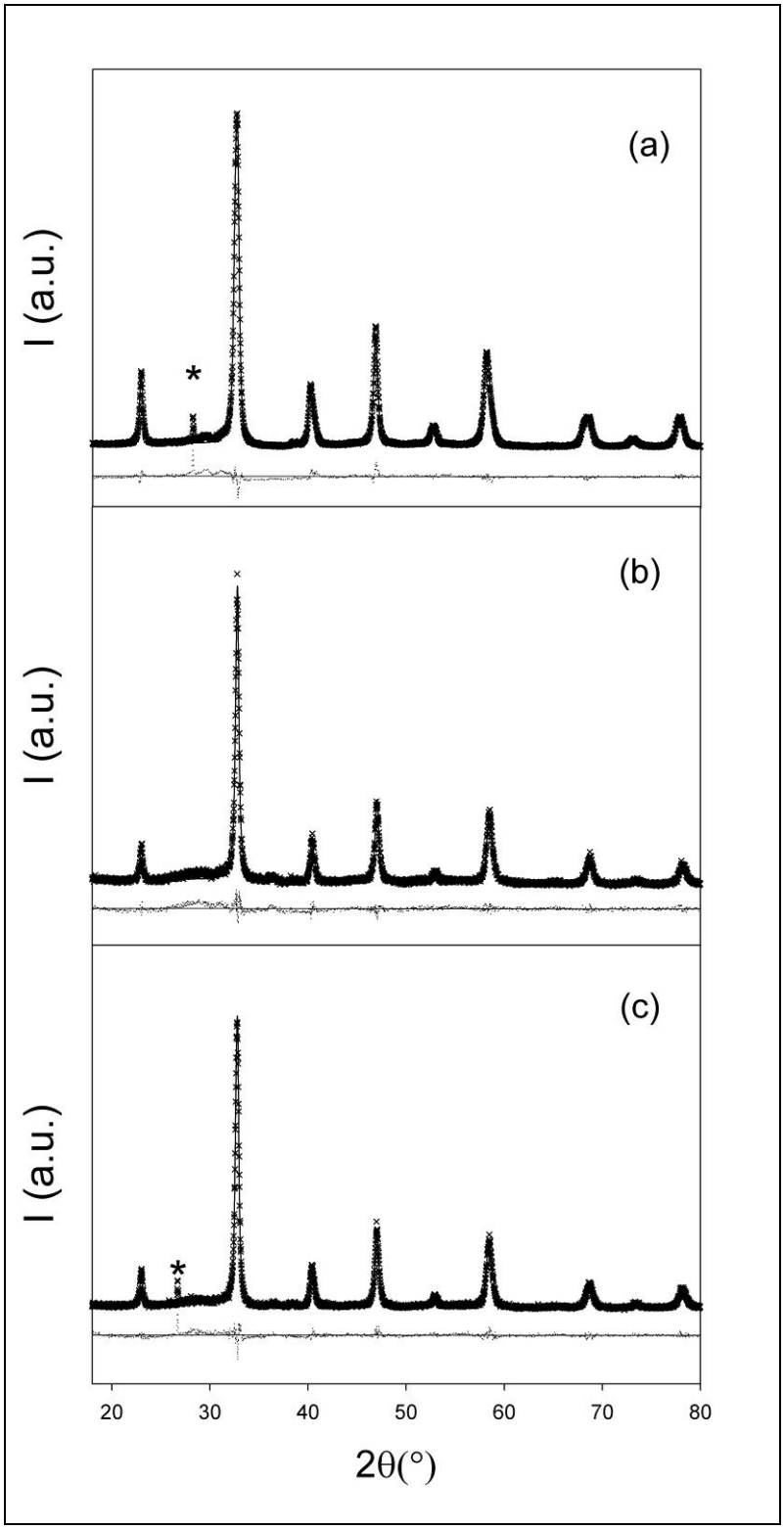

Fig. 3

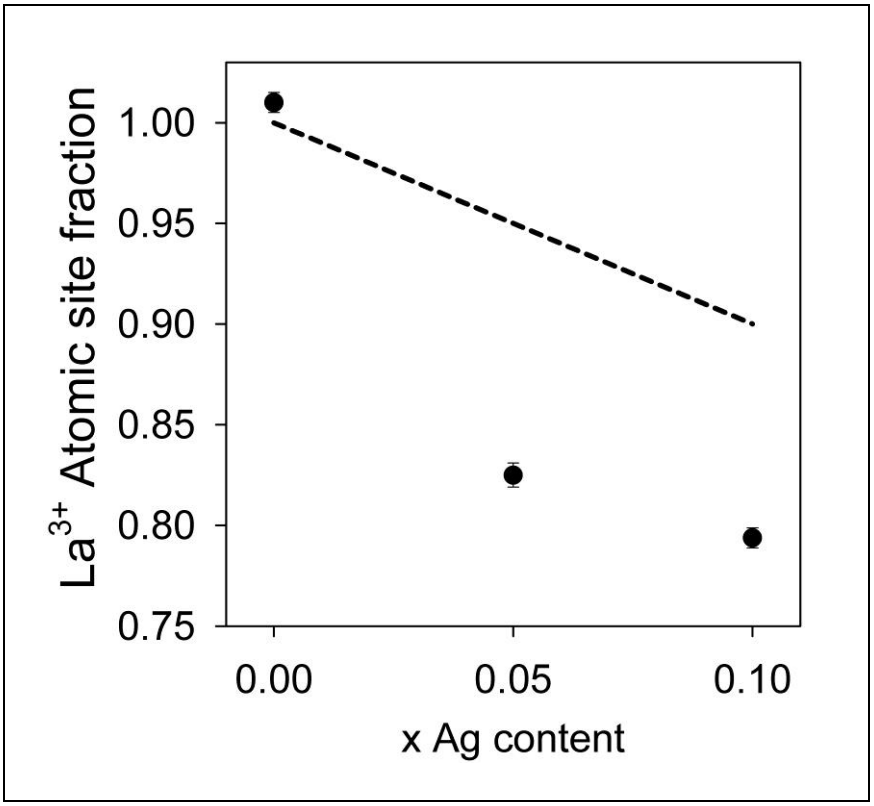
La3+ Atomic site fraction
1.00
0.95
0.90
0.85
0.80
0.75
0.00
0.05
0.10
x Ag content

Fig. 4

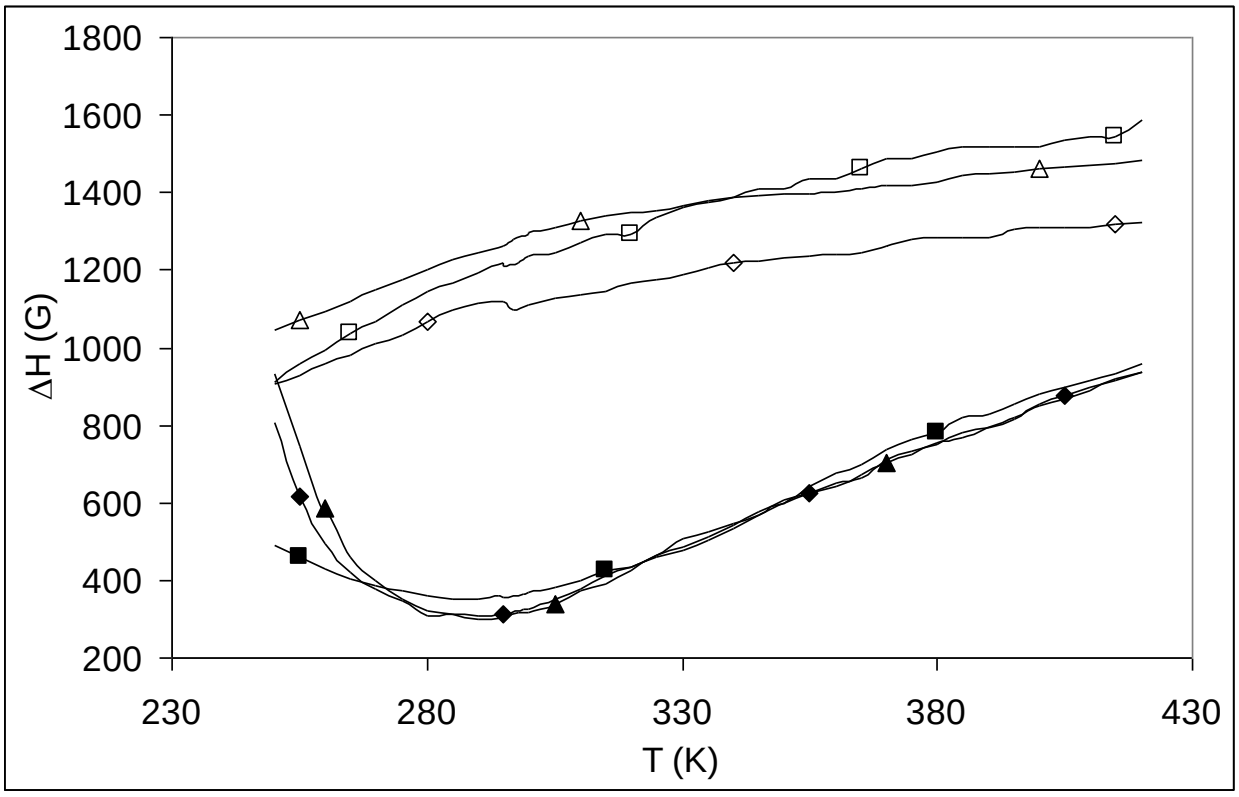
ΔH (G)
1800
1600
1400
1200
1000
800
600
400
200
230
280
330
380
430
T (K)

Fig 5a

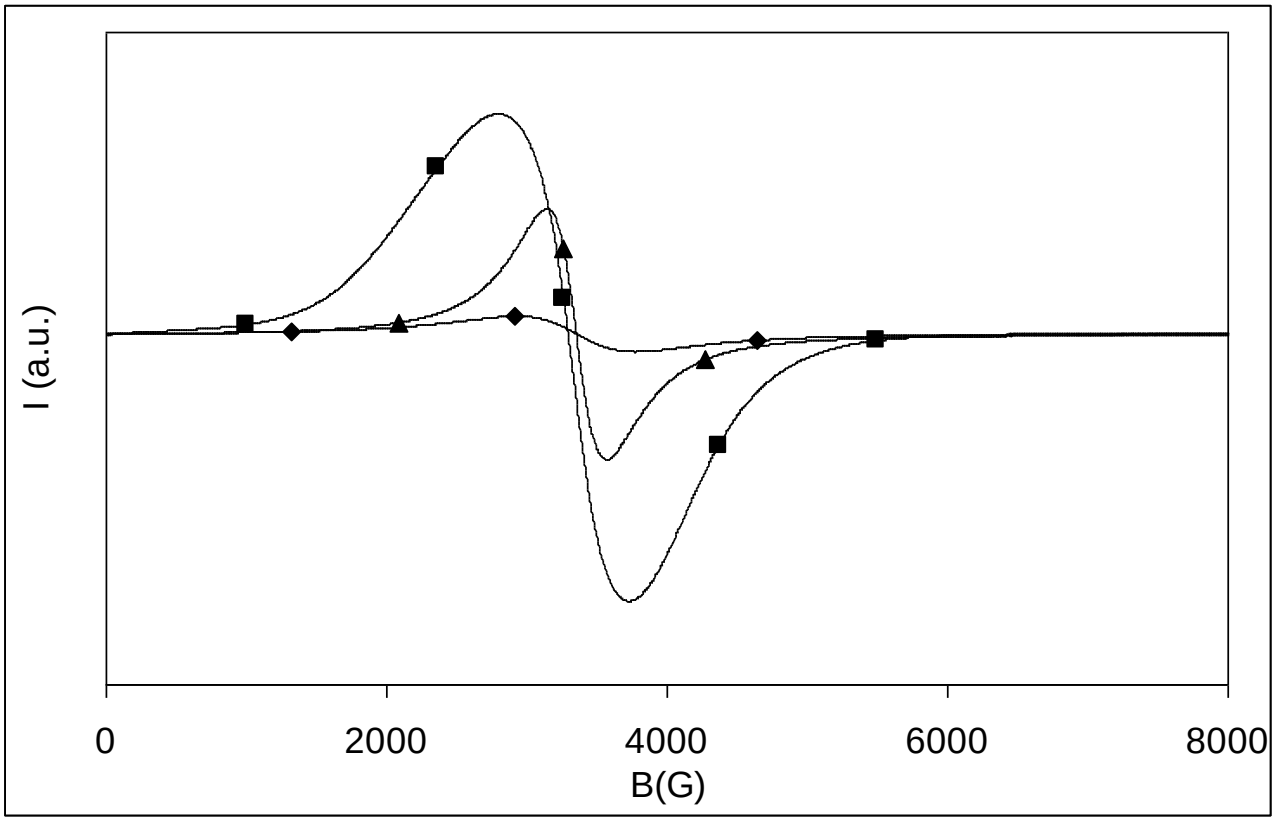

Fig. 5b

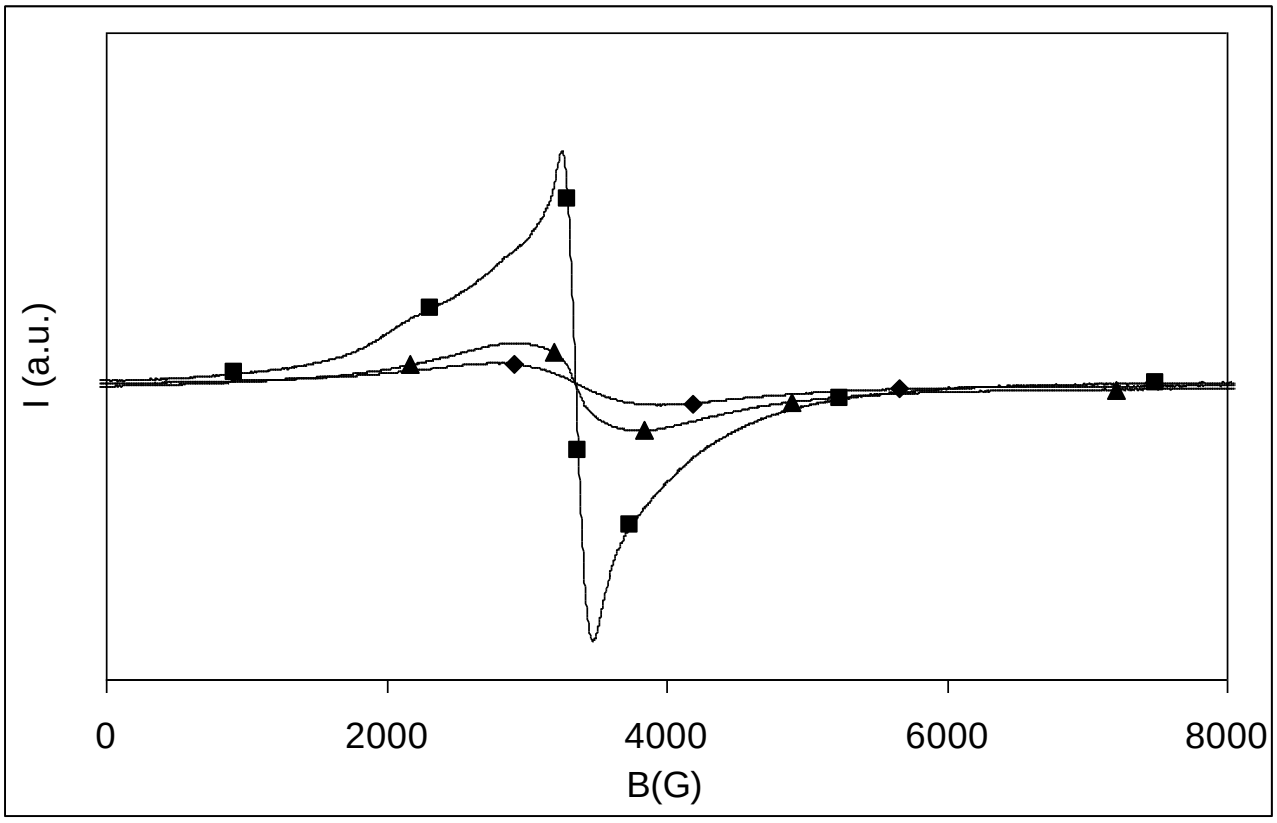

Fig. 6

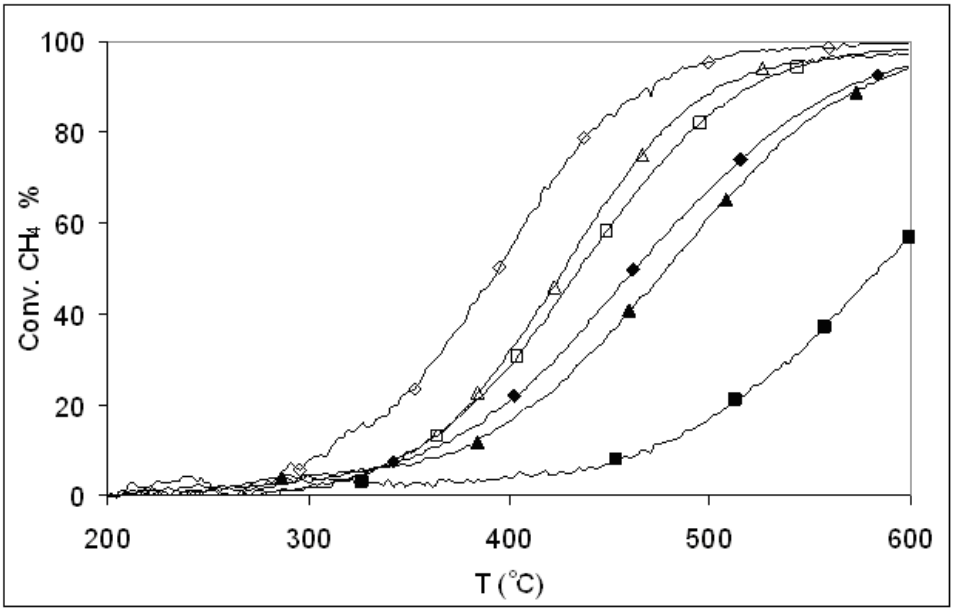
100
80
60
40
20
0
Conv. CH4 %
200
300
400
500
600
T (°C)

Fig. 7:

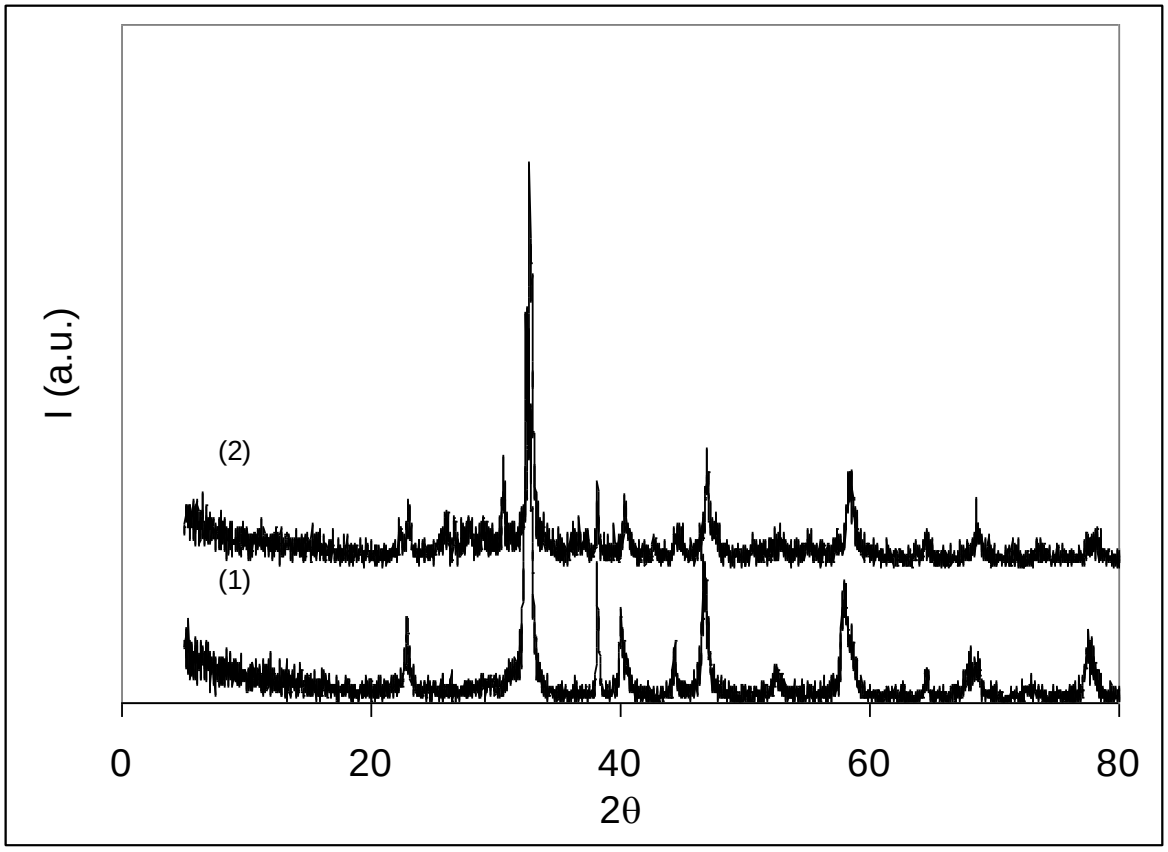
I (a.u.)
(2)
(1)
0
20
40
60
80
2θ

Fig. 8a

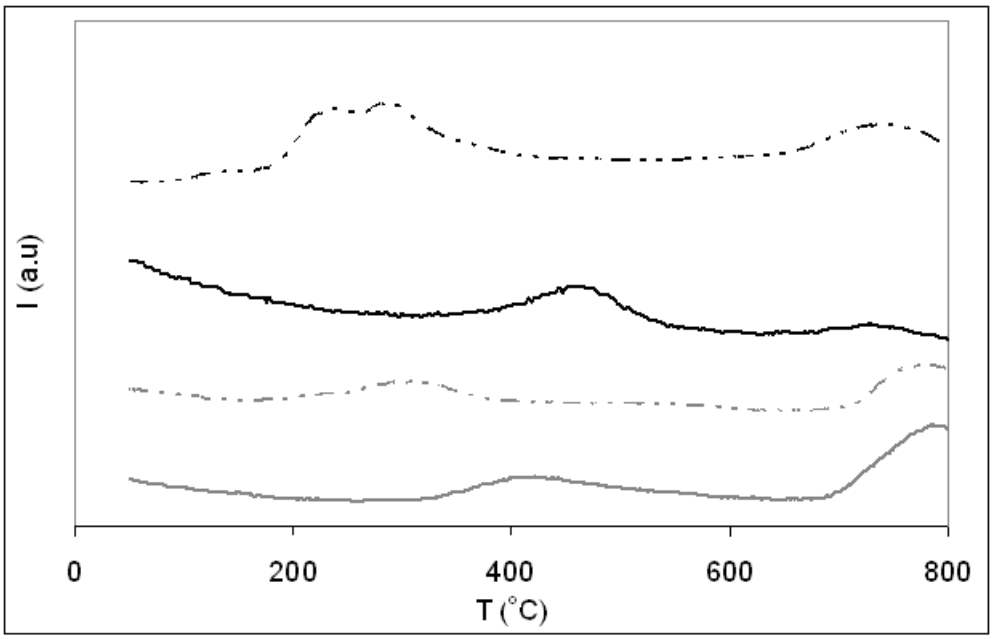

Fig. 8b

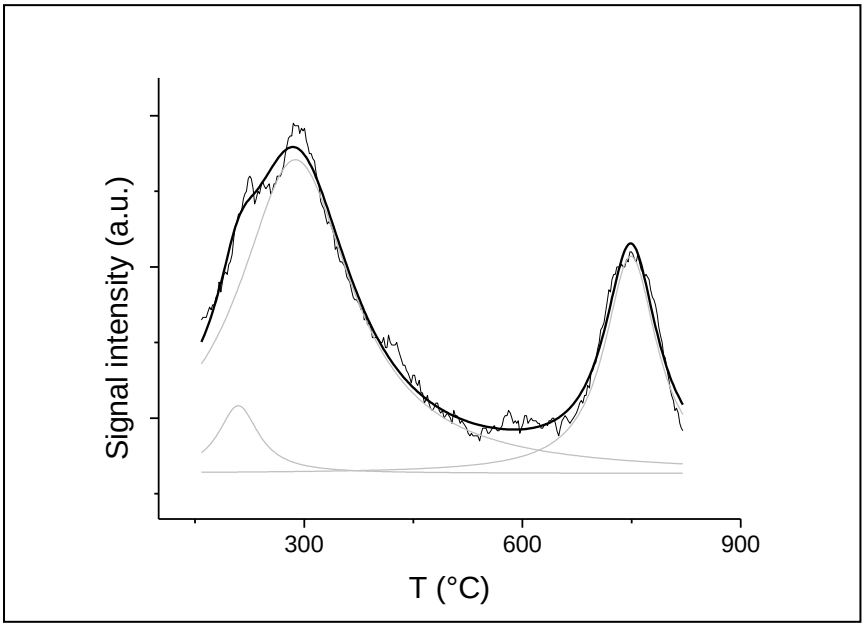

Fig. 9

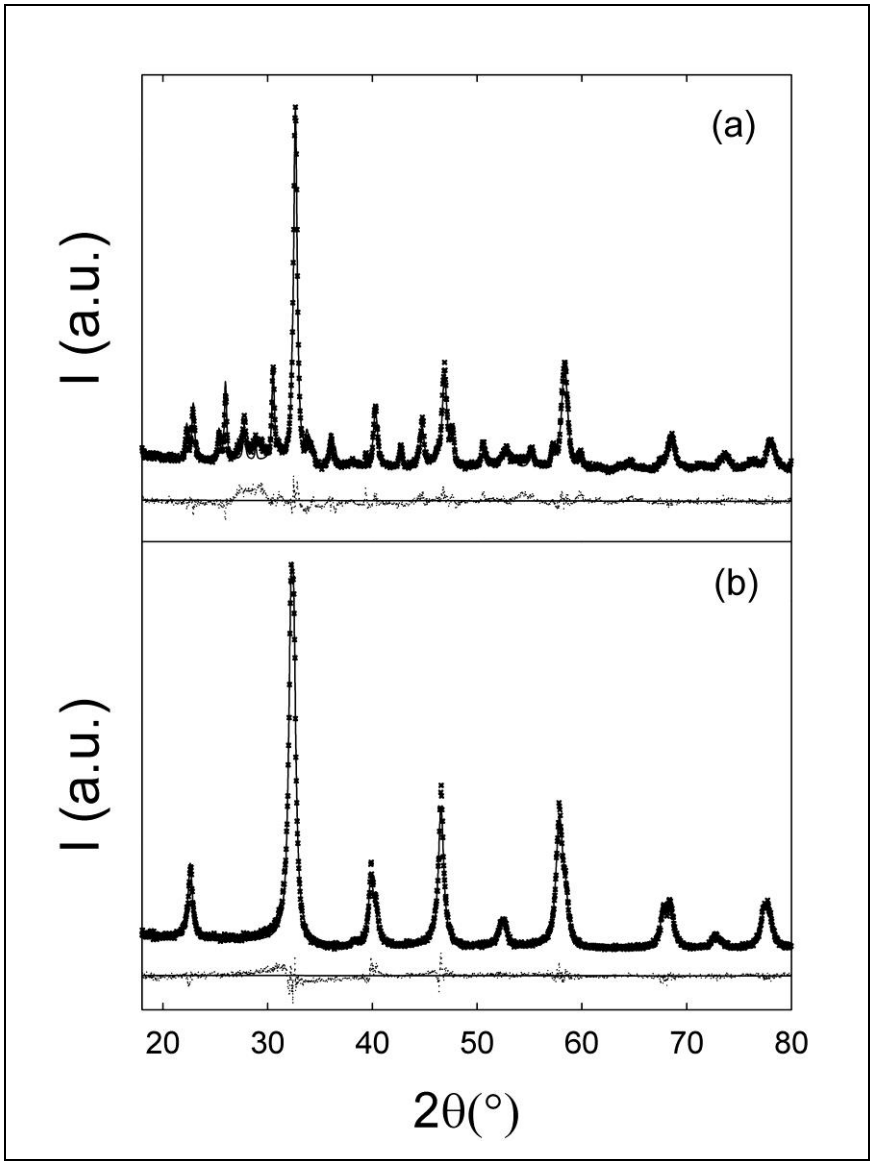

Fig. 10

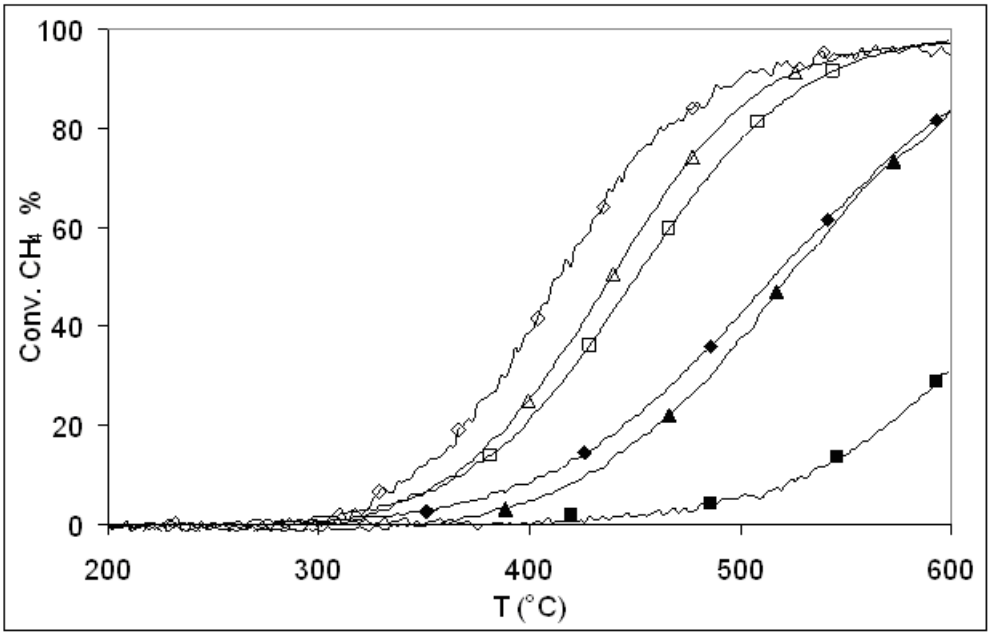
100
80
60
40
20
0
Conv. CH4 %
200
300
400
500
600
T (°C)

Fig. 11

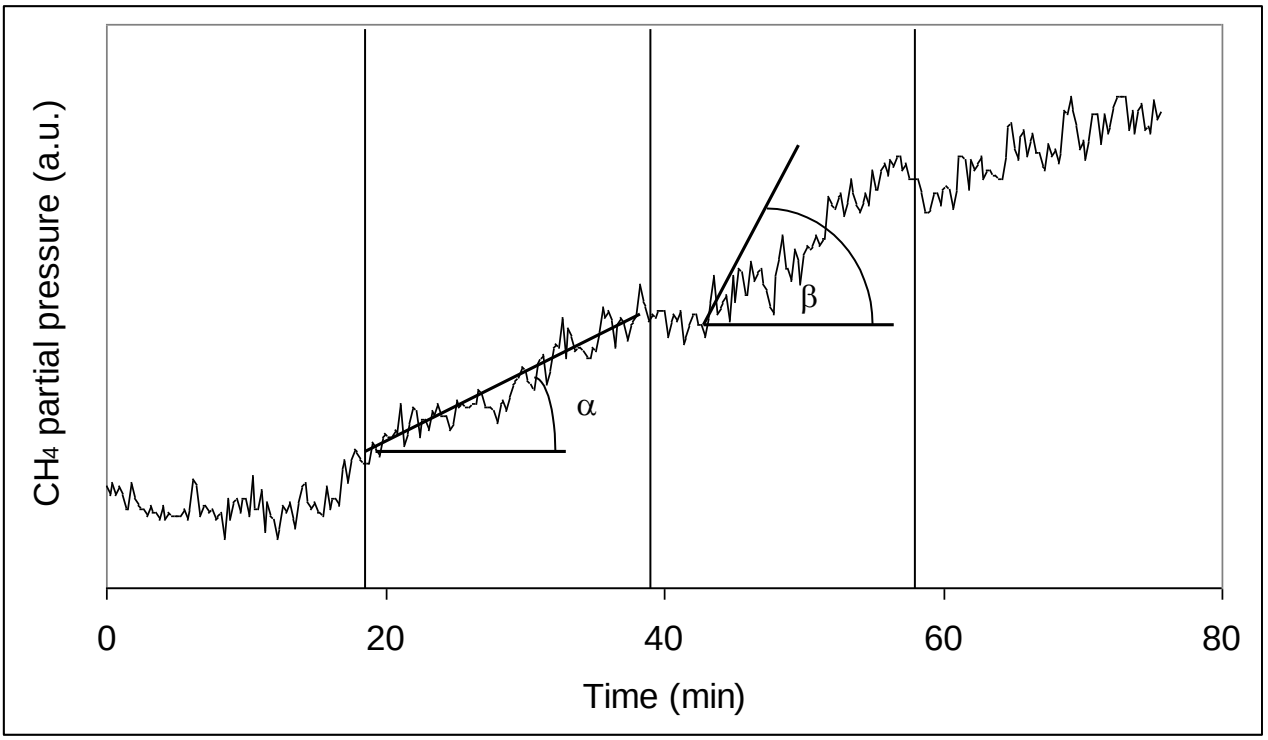
CH4 partial pressure (a.u.)
α
β
0
20
40
60
80
Time (min)